UWB-Based Localization System Considering Antenna Anisotropy and NLOS/Multipath Conditions

Taekyun Kim, Byoungkwon Yoon, and Dongjun Lee

Abstract— Ultra-wideband (UWB) communication technology has gained attention in robotics due to its ability to provide range measurements possibly with centimeter-level accuracy. Nevertheless, practical UWB range measurements are susceptible to disturbances from multiple sources, including the anisotropic characteristics of antennas, non-line-of-sight (NLOS) conditions, and multipath propagation. In this paper, we introduce a UWB range measurement model that addresses these sources of error. To accommodate the effects of antenna anisotropy, we adopt real spherical harmonics to represent directional bias in the UWB range measurement model. To handle delayed measurements induced by NLOS conditions and multipath propagation, an asymmetric heavy-tailed distribution is utilized to model the measurement noise. We calibrate this measurement model based on the maximum likelihood estimation method and propose a UWB-based localization system based on that. Our localization system provides: 1) anchor self-calibration, which identifies anchor placement by fusing visual-inertial-ranging measurements based on continuous-time state representation; and 2) filtering-based state estimation, which applies our measurement model into Kalman filtering framework via an iterative update algorithm. Experimental validation is conducted to demonstrate the effectiveness of the measurement model for our localization system. We open source our implementation of the proposed UWB-based localization system at `https://github.com/INRoL/inrol_uwb_localization`.

I. INTRODUCTION

In indoor environments where global navigation satellite systems (GNSS) are inaccessible to mobile robots, ultra-wideband (UWB) localization systems offer a suitable alternative [1]. These systems can achieve localization accuracy down to decimeter level. Their appeal lies in their cost-effectiveness, low power consumption, and ease of setup for lightweight systems, without the need for heavy computational resources. These advantages are particularly well-suited for mobile robots with limited resources and payload capacity. Furthermore, as they can provide information associated with globally fixed landmarks, the UWB range measurements have been applied to resolve a challenge of drift accumulated in long-horizon state estimation methods using exteroceptive sensors (e.g. camera [2, 3], LiDAR [4]).

Taekyun Kim, Byoungkwon Yoon, and Dongjun Lee are with the Department of Mechanical Engineering, IAMD and IOER, Seoul National University, Seoul 08826, Republic of Korea (e-mail: ktk4532@snu.ac.kr; dbss1126@snu.ac.kr; djlee@snu.ac.kr). Corresponding author: Dongjun Lee
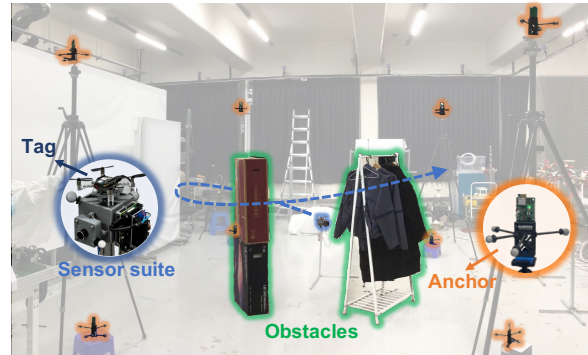
Fig. 1. The experiment setup for the UWB-based localization system.

UWB transceivers in localization systems are typically classified into two types: 1) the *tag* which is a UWB module attached to mobile platforms; and 2) the *anchors* which are multiple UWB modules deployed in the environment, as shown in Fig. 1. In the two-way ranging (TWR) technique, the tag measures the time-of-flight of the signal to an anchor by sending and receiving signals, then calculates the distance by multiplying the time interval with the speed of light.

To ensure the accuracy of the ranging technique, accurate timing measurements of signal transmission and reception are crucial. Even a timing error as small as one nanosecond can result in a ranging error of almost 30 centimeters. In this paper, we address the following sources of timing errors:

1) Anisotropic characteristics of antennas: Due to the anisotropic characteristics of UWB antennas, signal waveform distortion may occur depending on the angle of the line-of-sight [5]. The timing error resulting from these distortions manifest as an error pattern in range measurements [6], [7], which we refer to as *directional bias* in this paper.

2) Non-line-of-sight conditions and multipath propagation: Non-line-of-sight (NLOS) refers to situations where obstacles obstruct the direct line of sight between the UWB transmitter and receiver, resulting in waveform distortions in the UWB signal. Multipath propagation occurs when UWB signals reach the receiver through various routes, resulting in transmission delays and waveform distortion.

Recent studies have introduced new UWB range measurement models to mitigate these error sources. For instance, in [8] and [9], the directional bias is represented using a sparse Gaussian process. However, this model may not be practical for real-time systems with limited computational resource due to its time complexity. To address this challenge, the authors of [10] and [11] employ a computationally efficient neural network to model the bias. Nevertheless, this model, while more efficient, requires quite a substantial

number of parameters to capture the bias. Furthermore, due to the complexity of calculating the gradient of these models, it becomes challenging to utilize them in optimization-based estimation methods, which are widely employed for sensor fusion. For NLOS conditions and multipath propagation, a robust kernel is employed in [11] to alleviate the effect of outliers in UWB measurements. Additionally, alternative approaches surveyed in [12] identify these conditions based on range estimates or channel statistics.

In this paper, we utilize a directional bias model based on real spherical harmonics, which naturally represents a function defined on a spherical surface. In [13], a bias model utilizing real spherical harmonics is applied in a micro aerial vehicle localization system, yet it neglects the effect of anchor antenna. In contrast, we consider the effect of anchor antenna in this paper by introducing an additional bias function dependent on the line-of-sight angle in the anchor's frame. Additionally, to capture the influence of NLOS and multipath, we adopt an asymmetric heavy-tailed distribution [14] for the uncertainty model under the assumption that NLOS and multipath conditions result in positive errors in time-of-flight measurements.

We calibrate the proposed measurement model, including the directional bias functions and the noise model, based on the maximum likelihood estimation method. Based on our measurement model, we also propose an open-sourced UWB-based localization system with the following practically useful capabilities:

1) Anchor self-calibration: Once anchors are installed in the environment, their precise placement is essential for UWB-based localization. Manual calibration can be time-consuming and error-prone, necessitating automatic identification methods for anchor placement, often referred to as *anchor self-calibration* [15]. Recent researches have explored methods that concurrently estimate anchor placement and mobile robot state by using visual-inertial data (e.g. [3], [16], [17]). While these methods typically approach the SLAM problem in discrete-time, our contribution lies in developing a framework for anchor self-calibration based on continuous-time state representation which can effectively handle high-rate and asynchronous sensor data.

2) Filtering-based state estimation: Kalman filter is widely employed for real-time state estimation of mobile robots, operating under the assumption of Gaussian distribution for measurement noise. To accommodate our measurement model, which involves non-Gaussian noise, we introduce an iterative algorithm for the update step of the Kalman filter. This algorithm allows for the integration of our measurement model into Kalman filtering framework.

To our best knowledge, this is the only publically-available UWB-based localization system which provides measurement model calibration, anchor self-calibration, and filtering-based state estimation, considering anisotropy of antennas and NLOS/multipath conditions. Through our extensive experimental validation, we demonstrate the effectiveness of our model in 1) accurately capturing the UWB measurement bias and uncertainty; and 2) improving the accuracy of both
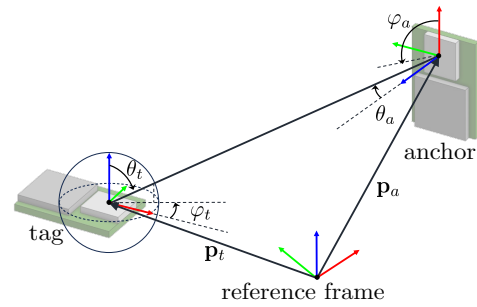

Fig. 2. The coordinate systems of the tag, the anchor, and the reference frame. The line-of-sight angles in the tag and the anchor coordinate are respectively expressed by (φ_t, θ_t) and (φ_a, θ_a)

anchor self-calibration and filtering-based state estimation results.

The rest of this paper is organized as follows. Section II will describe the proposed UWB range measurement model and its calibration technique. Then, in Section III and Section IV, we will provide an anchor self-calibration method and filtering-based state estimation method based on our measurement model. Experimental results are presented in Section V, followed by some concluding remarks in Section VI.

II. MEASUREMENT MODEL

This section introduces a novel UWB range measurement model aimed at enhancing the estimation performance, along with its calibration method. In the TWR technique, UWB range measurements are typically represented by the true distance between UWB modules with an additive zero-mean Gaussian noise $n_{\text{UWB}} \sim \mathcal{N}(0, \sigma^2)$, expressed as follows:

$$y = \|\mathbf{p}_t - \mathbf{p}_a\| + n_{\text{UWB}}, \tag{1}$$

where $y \geq 0$ is the value of the measured range, and $\mathbf{p}_t$, $\mathbf{p}_a \in \mathbb{R}^3$ denote the positions of the tag and the anchor, respectively, as illustrated in Fig. 2. In contrast to this standard model, our range measurement model considers several characteristics of UWB range measurements by integrating the following terms: 1) two directional bias functions capturing the anisotropic characteristics of both the tag and anchor antennas; and 2) a noise term reflecting the effect of the NLOS condition and multipath propagation.

A. Directional Bias Function

Waveform distortion, dependent on line-of-sight angles in UWB communications, results in directional bias in UWB range measurements [6], [7]. As shown in Fig. 2, the line-of-sight angles in the tag and the anchor coordinates can be expressed as two pairs of azimuth and elevation angles: (φ_t, θ_t), (φ_a, θ_a). Under the assumption that the tag and the anchor antennas affect range measurements independently, we represent the directional bias in UWB measurements as two scalar functions, $b_t(\varphi_t, \theta_t)$ and $b_a(\varphi_a, \theta_a)$, defined on a unit sphere $\mathbb{S}^2$. In this work, we assume that anchors with the same type of antenna exhibit the same bias pattern, and therefore have identical bias functions.

To represent these directional bias functions, we adopt spherical polynomials based on the real spherical harmonic

function $Y_{k,m}(\varphi, \theta)$, which can approximate a continuous scalar function on the unit sphere [18]:

$$b_t(\varphi, \theta) = \sum_{k=0}^{K} \sum_{m=-k}^{k} c_{k,m}^t Y_{k,m}(\varphi, \theta), \qquad (2)$$

$$b_a(\varphi, \theta) = \sum_{k=1}^{K} \sum_{m=-k}^{k} c_{k,m}^a Y_{k,m}(\varphi, \theta), \qquad (3)$$

where K denotes the degree of polynomials and $c_{k,m}^*$ represent the coefficients of each polynomial. The real spherical harmonic function $Y_{k,m} : \mathbb{S}^2 \to \mathbb{R}$ has an explicit form of

$$Y_{k,m} = \begin{cases} (-1)^m \sqrt{2} N_k^m \cos(m\varphi) P_k^m(\cos\theta) & m > 0 \\ (-1)^m \sqrt{2} N_k^m \sin(-m\varphi) P_k^{-m}(\cos\theta) & m < 0 \\ N_k^0 P_k^0(\cos\theta) & m = 0 \end{cases}$$

where k is the degree, m is the order of harmonic function, P_k^m are the associated Legendre polynomials and $N_k^m = \sqrt{\frac{2k+1}{4\pi} \frac{(k-|m|)!}{(k+|m|)!}}$ is a normalization term. Because $Y_{0,0}(\varphi, \theta)$ is a constant function, the anchor bias function (3) excludes $Y_{0,0}(\varphi, \theta)$ to prevent duplication of the constant term present in the tag bias function (2). The bias functions in (2) and (3) are determined by a total of $2K^2 + 4K + 1$ coefficients, including $c_{k,m}^t$ and $c_{k,m}^a$. A parameter set $\mathbf{\Theta}_c$, containing the coefficients of the bias functions, is defined as follows:

$$\mathbf{\Theta}_c := \{ c_{0,0}^t, c_{1,-1}^t, \cdots, c_{K,K}^t, c_{1,-1}^a, \cdots, c_{K,K}^a \}. \quad (4)$$

Using $b_t(\varphi, \theta)$ in (2) and $b_a(\varphi, \theta)$ in (3), we improve the standard UWB range measurement model in (1) as:

$$y = \|\mathbf{p}_t - \mathbf{p}_a\| + b_t(\varphi_t, \theta_t) + b_a(\varphi_a, \theta_a) + n_{\text{UWB}}, \quad (5)$$

where the noise term, n_{uwb}, represents the measurement uncertainty, which will be further discussed in Section II-B. Using the parameters $\mathbf{\Theta}_c$, we define a measurement function for the deterministic term of the model as follows:

$$h_{\text{UWB}}(\mathbf{T}_a^t; \mathbf{\Theta}_c) := \|\mathbf{p}_t - \mathbf{p}_a\| + b_t(\varphi_t, \theta_t) + b_a(\varphi_a, \theta_a), \quad (6)$$

where $\mathbf{T}_a^t \in \mathrm{SE}(3)$ represents the pose of the anchor in the tag coordinate system. From the relative pose $\mathbf{T}_a^t$, we can calculate the distance ($\|\mathbf{p}_t - \mathbf{p}_a\|$) and the line-of-sight angles ($\varphi_t, \theta_t, \varphi_a, \theta_a$).

B. Noise Model

NLOS conditions and multipath propagation can cause delays in UWB signals, leading to positive errors in range measurements. To accommodate their delaying effect on measurements, we utilize an asymmetric heavy-tailed noise distribution, which is applied to model outliers in UWB measurements [14]:

$$n_{\text{UWB}} \sim \begin{cases} (2-\alpha)\mathcal{N}(0, \sigma^2), & \text{for } n_{\text{UWB}} < 0, \\ \alpha \text{Cauchy}(0, \gamma), & \text{for } n_{\text{UWB}} \geq 0, \end{cases} \quad (7)$$

where σ is the standard deviation of the Gaussian distribution for negative values, γ is the scale parameter of the Cauchy distribution for positive values, and the constants α and

$2 - \alpha$ are introduced to ensure the integral of a probability density function equals one. From the continuity condition at $n_{\text{UWB}} = 0$, the parameter α is determined by σ and γ [14]. Thus, we denote the parameters representing the asymmetric noise distribution as $\mathbf{\Theta}_n := \{\sigma, \gamma\}$. The negative log likelihood function for the asymmetric noise distribution (7) is derived as follows:

$$\rho(n_{\text{UWB}}; \mathbf{\Theta}_n) := \begin{cases} \mathcal{L}_G, & \text{for } n_{\text{UWB}} < 0, \\ \mathcal{L}_C, & \text{for } n_{\text{UWB}} \geq 0, \end{cases} \quad (8)$$

$$\mathcal{L}_G := -\log(2-\alpha) + \frac{1}{2}\log 2\pi + \log\sigma + \frac{n_{\text{UWB}}^2}{2\sigma^2}, \quad (9)$$

$$\mathcal{L}_C := -\log\alpha + \log\pi + \log\gamma + \log(1 + \frac{n_{\text{UWB}}^2}{\gamma^2}). \quad (10)$$

C. Measurement Model Calibration

This subsection presents a calibration method for the model parameters $\mathbf{\Theta}_c$ and $\mathbf{\Theta}_n$. We collect the calibration dataset by measuring range while recording the relative pose between a moving tag and fixed anchors. The dataset is denoted as $\{(y_1, \mathbf{T}_{a,1}^t), \cdots, (y_N, \mathbf{T}_{a,N}^t)\}$, where $\mathbf{T}_{a,i}^t$ represents the relative pose of the tag and the anchor for the i-th measurement. Using the UWB range measurement model in (5), we formulate an optimization problem for calibrating the model parameters based on the maximum likelihood estimation as follows:

$$\min_{\mathbf{\Theta}_c, \mathbf{\Theta}_n} \sum_{i=1}^{N} \rho(e_i; \mathbf{\Theta}_n), \quad (11)$$

$$e_i := y_i - h_{\text{UWB}}(\mathbf{T}_{a,i}^t; \mathbf{\Theta}_c), \quad (12)$$

where e_i denote the measurement errors determined by the parameter $\mathbf{\Theta}_c$.

III. ANCHOR SELF-CALIBRATION

In this section, we introduce an anchor self-calibration method utilizing the measurement model outlined in (5). Our method leverages the tightly coupled fusion of visual, inertial and UWB measurements within a mobile platform. To effectively handle the high-rate and asynchronous sensor data, we employ a continuous-time state representation. Inspired by the continuous-time vision-based SLAM method in [19], we propose a framework to solve the estimation problem, comprising a multi-step initialization process and a full-batch optimization.

The proposed anchor self-calibration method simultaneously estimates a continuous-time state variable $\mathbf{x}(t)$ and landmark variables consisting of N_f positions of image feature points $\mathcal{P}_f = \{\mathbf{p}_{f_1}, \cdots, \mathbf{p}_{f_{N_f}}\}$ and N_a poses of installed anchors $\mathcal{T}_a = \{\mathbf{T}_{a_1}, \cdots, \mathbf{T}_{a_{N_a}}\}$, where $\mathbf{p}_{f_i} \in \mathbb{R}^3$ and $\mathbf{T}_{a_i} \in \mathrm{SE}(3)$. The state $\mathbf{x}(t)$ contains the position $\mathbf{p}(t) \in \mathbb{R}^3$ and orientation $\mathbf{R}(t) \in \mathrm{SO}(3)$ of the trajectory under estimation, along with the time-varying accelerometer/gyroscope biases $\mathbf{b}_\alpha(t), \mathbf{b}_\omega(t) \in \mathbb{R}^3$.

We parameterize the continuous-time state by cumulative B-splines [20], which includes three-dimensional vector elements $(\mathbf{p}(t), \mathbf{b}_\alpha(t), \mathbf{b}_\omega(t))$ and a Lie group element $(\mathbf{R}(t))$.

In the B-spline representation, these elements are represented by control nodes distributed uniformly over a time interval.

A. Initialization

We first obtain scaleless camera poses $\{\mathbf{p}_{c_j}, \mathbf{R}_{c_j}\}$ with $j \in \{1, 2, \cdots, N_c\}$ and 3D feature point positions by using monocular structure-from-motion (SfM) software such as COLMAP [21]. Next, we fit B-splines of position and orientation to the N_c camera poses by minimizing the position and orientation error as follows:

$$\min_{\mathbf{p}_c(t), \mathbf{R}_c(t)} \sum_{j=0}^{N_c} \|\mathbf{p}_c(t_j) - \mathbf{p}_{c_j}\|^2 + \|\mathrm{Log}(\mathbf{R}_c(t_j)^T \mathbf{R}_{c_j})\|^2, \tag{13}$$

where $\mathrm{Log}(\cdot)$ is the logarithm map of SO(3), and $(\mathbf{p}_c(t_j), \mathbf{R}_c(t_j))$ are the samples of the B-splines at the timestamp of the j-th camera pose. The initial values of the control nodes at times $t_i = t_0 + i\Delta t$ for the B-splines are obtained by linear interpolation of the camera poses, where t_0 is the time of the first camera pose and Δt is the uniform time interval between the adjacent control nodes.

The subsequent phase of our framework involves finding the scale s of the B-splines and an initial estimate of anchor positions $\mathcal{P}_a = \{\mathbf{p}_{a_1}, \cdots, \mathbf{p}_{a_{N_a}}\}$ utilizing UWB measurements $\{y_1, \cdots, y_{N_u}\}$. We accomplish this by minimizing the residuals of UWB measurements, formulated as follows:

$$\min_{s, \mathcal{P}_a} \sum_{i=1}^{N_u} \|y_i - d_i\|^2, \tag{14}$$

$$d_i := \|\mathbf{p}_{a_{\kappa_i}} - \mathbf{p}_t(t_i)\|, \tag{15}$$

where $\kappa_i \in \{1, \cdots, N_a\}$ is the anchor index associated with a measurement y_i and the sampled tag positions are defined as $\mathbf{p}_t(t_i) = s\mathbf{p}_c(t_i) + \mathbf{R}_c(t_i)\mathbf{p}_t^c$, where $\mathbf{p}_t^c$ is the tag position in the camera coordinate system. From the estimated scale s, we can derive an initial estimate of the scaled B-spline trajectory $(\mathbf{p}_c(t), \mathbf{R}_c(t))$ and the scaled position of feature points $\mathcal{P}_f$. These estimation results are refined in the subsequent full-batch optimization process.

B. Full-batch Optimization

In the full-batch optimization, we estimate a state vector $\mathcal{X}$ defined by $\mathcal{X} := \{\mathbf{x}(t), \mathcal{P}_f, \mathcal{T}_a, \mathbf{g}\}$, where $\mathbf{g}$ denotes the gravity vector with a magnitude of $9.81\mathrm{m/s}^2$. In this paper, accelerometer and gyroscope measurements are represented as $\boldsymbol{\alpha}_k$ and $\boldsymbol{\varpi}_k$, respectively, which are obtained at times $t_k \in \{t_1, \cdots, t_{N_k}\}$. The image feature measurement $\mathbf{z}_{jm}$ refers to the pixel location of the feature point $\mathbf{p}_{f_m}$ observed in the j-th image. For visual and inertial measurements, we use the standard IMU and camera model outlined below:

$$\mathbf{z}_{jm} := \pi\left(\mathbf{R}_c(t_m)^T(\mathbf{p}_{f_m} - \mathbf{p}_c(t_j))\right) + \mathbf{n}_z, \tag{16}$$

$$\boldsymbol{\alpha}_k := \mathbf{R}_b(t_k)^T(\ddot{\mathbf{p}}_b(t_k) - \mathbf{g}) + \mathbf{b}_\alpha(t_k) + \mathbf{n}_\alpha, \tag{17}$$

$$\boldsymbol{\varpi}_k := \mathbf{R}_b(t_k)^T\boldsymbol{\omega}_b(t_k) + \mathbf{b}_\omega(t_k) + \mathbf{n}_\omega, \tag{18}$$

where each noise term $\mathbf{n}_*$ follows a Gaussian distribution of $\mathcal{N}(0, \boldsymbol{\Sigma}_*)$, and $\pi(\cdot)$ denotes any nonlinear camera projection

function mapping a 3D point to the pixel location. We represent the accelerometer and gyroscope biases as zero-mean white Gaussian processes described by:

$$\dot{\mathbf{b}}_\alpha(t) = \mathbf{w}_\alpha(t) \quad \mathbf{w}_\alpha(t) \sim \mathcal{GP}(\mathbf{0}, \mathbf{Q}_\alpha\delta(t - t')), \tag{19}$$

$$\dot{\mathbf{b}}_\omega(t) = \mathbf{w}_\omega(t) \quad \mathbf{w}_\omega(t) \sim \mathcal{GP}(\mathbf{0}, \mathbf{Q}_\omega\delta(t - t')), \tag{20}$$

under the assumption that these processes are statistically independent. From the measurement models, we define each measurement residual as follows:

$$e_{y_i} := y_i - h_{\mathrm{UWB}}(\mathbf{T}_t^{-1}\mathbf{T}_{a_{\kappa_i}}; \boldsymbol{\Theta}_c), \tag{21}$$

$$\mathbf{e}_{z_{jm}} := \mathbf{z}_{jm} - \pi\left(\mathbf{R}_c(t_j)^T(\mathbf{p}_{f_m} - \mathbf{p}_c(t_j))\right), \tag{22}$$

$$\mathbf{e}_{\alpha_k} := \boldsymbol{\alpha}_k - \mathbf{R}_b(t_k)^T(\ddot{\mathbf{p}}_b(t_k) - \mathbf{g}) - \mathbf{b}_\alpha(t_k), \tag{23}$$

$$\mathbf{e}_{\omega_k} := \boldsymbol{\varpi}_k - \mathbf{R}_b(t_k)^T\boldsymbol{\omega}_b(t_k) - \mathbf{b}_\omega(t_k). \tag{24}$$

Since the effect of the anchor orientation on the range measurement model is much smaller than the distance term, the available information for estimating them is relatively limited. Fortunately, obtaining prior information on the orientation of anchors is typically straightforward. Therefore, we can incorporate this prior information by modeling it as

$$\mathbf{R}_j = \mathbf{R}_{j,p}\mathrm{Exp}(\mathbf{n}_p), \quad \mathbf{n}_p \sim \mathcal{N}(0, \boldsymbol{\Sigma}_p), \tag{25}$$

where $\mathbf{R}_j, \mathbf{R}_{j,p}$ denote respectively the estimated orientation and the prior orientation of the j-th anchor, respectively. Here, $\mathbf{n}_p \in \mathbb{R}^3$ is a Gaussian noise vector, and $\mathrm{Exp}(\cdot)$ denotes the exponential map of SO(3).

From the measurement models and the prior information, we can derive an optimization cost to estimate the state vector $\mathcal{X}$ as follows:

$$\begin{aligned}
\min_{\mathcal{X}} & \sum_{i=1}^{N_u} \rho(e_{y_i}; \boldsymbol{\Theta}_n) + \frac{1}{2}\sum_{j=1}^{N_c}\sum_{m \in \mathcal{I}_j} \|\mathbf{e}_{z_{jm}}\|^2_{\boldsymbol{\Sigma}_z^{-1}} \\
& + \frac{1}{2}\sum_{k=1}^{N_k}\left(\|\mathbf{e}_{\alpha_k}\|^2_{\boldsymbol{\Sigma}_\alpha^{-1}} + \|\mathbf{e}_{\omega_k}\|^2_{\boldsymbol{\Sigma}_\omega^{-1}}\right) \\
& + \frac{1}{2}\int_{t_0}^{t_{N_k}}\left(\|\dot{\mathbf{b}}_\alpha(\tau)\|^2_{\mathbf{Q}_\alpha^{-1}} + \|\dot{\mathbf{b}}_\omega(\tau)\|^2_{\mathbf{Q}_\omega^{-1}}\right)d\tau \\
& + \frac{1}{2}\sum_{j=1}^{N_a}\|\mathrm{Log}(\mathbf{R}_{j,p}^T\mathbf{R}_j)\|^2_{\boldsymbol{\Sigma}_p^{-1}},
\end{aligned} \tag{26}$$

where $\mathcal{I}_j \subset \{1, \cdots, N_f\}$ denotes the subset of feature point indices observed in the j-th image.

Note that the estimated results are expressed in the coordinate system defined by the SfM software. Therefore, to use the anchor placement in real-time state estimation, it may be necessary to align them with a desired reference coordinate system.

IV. FILTERING-BASED STATE ESTIMATION

While state estimation methods based on the extended Kalman filter are commonly used for mobile robots, our measurement model cannot be directly applied to them due to its non-Gaussian noise model. In this section, we present a method of integrating our measurement model into Kalman filtering framework.

Consider a discrete system using the output variable y_k modeled by our UWB measurement model (5), which can be expressed by

$$y_k = h(\mathbf{x}_k) + n_{\text{UWB}}, \quad (27)$$

where $\mathbf{x}_k \in \mathbb{R}^n$ is the state vector of the system and $h(\cdot)$ is the rewritten measurement function in (6) for brevity. The update step of M-estimation based Kalman filter [22] for our system can be formulated as:

$$\hat{\mathbf{x}}_k^+ = \operatorname*{argmin}_{\mathbf{x}_k} \frac{1}{2}\|\mathbf{x}_k - \hat{\mathbf{x}}_k\|^2_{\mathbf{P}_k^{-1}} + \rho\left(e_{y_k}(\mathbf{x}_k); \mathbf{\Theta}_n\right), \quad (28)$$

with a prior information $\mathbf{x}_k \sim \mathcal{N}(\hat{\mathbf{x}}_k, \mathbf{P}_k)$ and $e_{y_k}(\mathbf{x}_k) := y_k - h(\mathbf{x}_k)$. For brevity, we will omit the noise parameter $\mathbf{\Theta}_n$, i.e., $\rho(e) = \rho(e; \mathbf{\Theta}_n)$.

By differentiating the cost function of (28), we can find a necessary condition of the solution, expressed as

$$\mathbf{P}_k^{-1}(\mathbf{x}_k - \hat{\mathbf{x}}_k) - (\frac{\partial h(\mathbf{x}_k)}{\partial \mathbf{x}_k})^T \psi(e_{y_k}(\mathbf{x}_k))e_{y_k}(\mathbf{x}_k) = 0 \quad (29)$$

with

$$\psi(e) := \frac{1}{e}\frac{\partial \rho(e)}{\partial e} = \begin{cases} \frac{1}{\sigma^2}, & \text{for } e < 0, \\ \frac{2}{\gamma^2 + e^2}, & \text{for } e \geq 0. \end{cases} \quad (30)$$

To find a solution of the equation (29), we propose an iterative algorithm. First, we set $\hat{\mathbf{x}}_{k,1} = \hat{\mathbf{x}}_k$ to initialize the algorithm. For brevity, we drop the timestep subscript k in the subsequent equations. In the l-th iteration, we approximate the equation (29) using a Taylor expansion around the current solution $\hat{\mathbf{x}}_l$ as

$$\mathbf{P}^{-1}(\mathbf{x} - \hat{\mathbf{x}}) - \mathbf{H}_l^T \psi(e_y(\mathbf{x}))(y - h(\hat{\mathbf{x}}_l) - \mathbf{H}_l(\mathbf{x} - \hat{\mathbf{x}}_l)) = 0, \quad (31)$$

$$\mathbf{H}_l := \frac{\partial h(\mathbf{x})}{\partial \mathbf{x}}\bigg|_{\hat{\mathbf{x}}_l} \in \mathbb{R}^{1 \times n}. \quad (32)$$

Then, we substitute the current solution $\hat{\mathbf{x}}_l$ into $\psi(e_y(\mathbf{x}))$ to obtain a new solution $\hat{\mathbf{x}}_{l+1}$ as follows:

$$\hat{\mathbf{x}}_{l+1} = \hat{\mathbf{x}} + \mathbf{K}_l(y - h(\hat{\mathbf{x}}_l) - \mathbf{H}_l(\hat{\mathbf{x}} - \hat{\mathbf{x}}_l)), \quad (33)$$

$$\mathbf{K}_l := \mathbf{P}\mathbf{H}_l^T(\psi_l^{-1} + \mathbf{H}_l\mathbf{P}\mathbf{H}_l^T)^{-1}, \quad (34)$$

with $\psi_l := \psi(e_y(\hat{\mathbf{x}}_l))$. After the convergence with L iterations, we can get a posterior state estimate as $\hat{\mathbf{x}}^+ = \hat{\mathbf{x}}_{L+1}$.

Although the posterior probability distribution is non-Gaussian due to the nonlinear measurement function and non-Gaussian noise model, we approximate it as a Gaussian distribution by using the Laplace approximation [23]. This involves computing the Hessian matrix of the cost function in (28).

First, the approximation of the second-order derivative of $\rho(e_y(\mathbf{x}))$ at the solution $\hat{\mathbf{x}}^+$ can be derived as $\mathbf{H}_{L+1}^T \psi_{L+1} \mathbf{H}_{L+1}$. Then, the posterior covariance matrix of the approximated Gaussian distribution can be obtained as

$$\mathbf{P}^+ = (\mathbf{P}^{-1} + \mathbf{H}_{L+1}^T \psi_{L+1} \mathbf{H}_{L+1})^{-1}. \quad (35)$$

Using the matrix inversion lemma, this can be written as

$$\begin{aligned} \mathbf{P}^+ &= \mathbf{P} - \mathbf{P}\mathbf{H}_{L+1}^T(\psi_L^{-1} + \mathbf{H}_{L+1}\mathbf{P}\mathbf{H}_{L+1}^T)^{-1}\mathbf{H}_{L+1}\mathbf{P} \\ &= (\mathbf{I} - \mathbf{K}_{L+1}\mathbf{H}_{L+1})\mathbf{P}. \end{aligned} \quad (36)$$
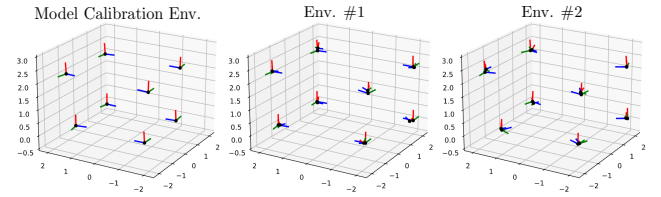

Fig. 3. The anchor setups in the experiments (left) for the measurement model calibration (Section. V-A); (middle) Env. #1; and (right) Env. #2 in the experiments of Section. V-B and Section. V-C. The larger frames indicate the ground truth pose of the anchors and the smaller ones indicate the anchor placement estimated by the proposed model.

TABLE I
CALIBRATED NOISE PARAMETERS AND RMSE OF THREE MEASUREMENT MODELS

Model	Calibrated noise parameters	RMSE
A	$\sigma = 0.153$	15.5cm
B	$\sigma = 0.127$	13.3cm
C	$\sigma = 0.090, \ \gamma = 0.048$	13.3cm

V. EXPERIMENTS

In this section, we validate the proposed UWB range measurement model experimentally and demonstrate its effectiveness within the UWB-based localization system. All sensor data were collected using a sensor suite, illustrated in Fig. 1. The suite comprises a monocular global shutter camera and a Crazyflie 2.1 nano-quadcopter capable of providing UWB range and IMU measurements at a rate of 100 Hz. For the UWB anchors in the environments, we employed eight Qorvo's DWM1001-DEV boards. The ground truth poses of both the sensor suite and the anchors were tracked by the OptiTrack MOCAP (motion capture) system at 100 Hz. Each set of experiment data was logged onto an onboard computer (Raspberry Pi 4) mounted on the sensor suite. To solve the optimization problems in the measurement calibration (Section V-A) and the anchor self-calibration (Section V-B), we utilized the Ceres solver [24].

To validate each component of the proposed measurement model, we used the following three measurement models:

1) Model **A**: The standard measurement model in (1).
2) Model **B** : A measurement model using the proposed directional bias functions (2), (3) with Gaussian noise.
3) Model **C** : Our proposed measurement model in (5).

A. UWB Range Measurement Model Calibration

To calibrate the measurement models, we collected a calibration dataset with 54,000 UWB range measurements and a test dataset with 22,000. These measurements were obtained as the sensor suite traversed through the anchor setup illustrated in Fig. 3. The relative poses between the tag and anchors were obtained using the MOCAP system. For each measurement model described above, the calibration was conducted using the maximum-likelihood estimation method outlined in Section. II-C. We experimentally determined the degree of the spherical polynomials K to be four, which provided sufficient accuracy for our setup.

We evaluate the calibration results by comparing the calibrated noise distribution with the measurement error
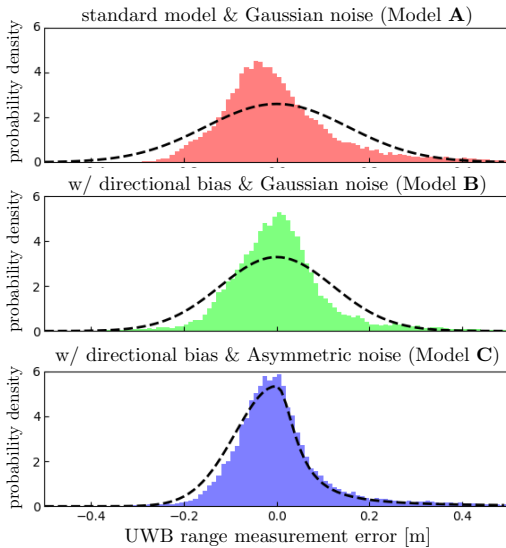
Fig. 4. The measurement error histogram computed by the calibration results of (top) model **A**; (middle) model **B**; and (bottom) model **C**. The dashed lines indicate the calibrated probability density functions of each measurement noise model.
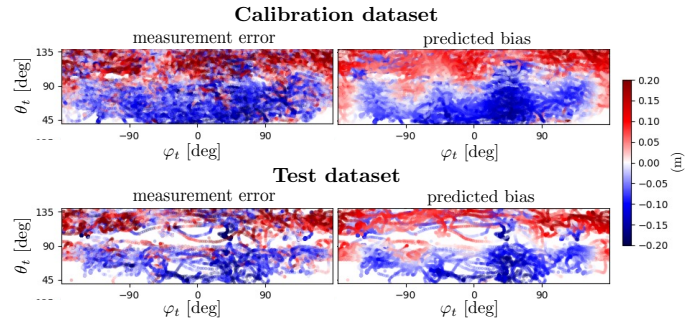

Fig. 5. Comparison of errors in UWB raw measurements (left) with the bias values predicted by model **C** for both the calibration dataset (top) and the test dataset (bottom), shown in the tag's spherical coordinate system.

Model	Env. #1		Env. #2	
	position	orientation	position	orientation
A	14.9cm	-	15.9cm	-
B	9.2cm	**30.3°**	9.2cm	**29.5°**
C	**8.7**cm	30.4°	**8.4**cm	38.9°

histogram derived from the test dataset, see Fig. 4. The calibrated noise parameters and root mean squared error of each measurement model can be found in Table I. The analysis reveals that model **B** and model **C** exhibits lower measurement errors compared to **A**, attributed to its compensation of antenna effects through directional bias functions. On the other hand, the calibration result of the model **C**, which incorporates an asymmetric heavy-tailed noise distribution, shows the closer match with the error histogram. This indicates that our proposed model effectively reflects the sources of error in range measurements. Additionally, Fig. 5 visually demonstrates that our model effectively reflects error patterns from the line-of-sight angles.

B. Anchor Self-calibration

To validate the proposed anchor self-calibration method, we gathered datasets in two environments: 1) an open space without obstacles (Env. #1); and 2) a space containing obstacles (Env. #2) to simulate stronger NLOS/multipath effects, which can be seen in Fig. 1. The anchor placement of both environments are shown in Fig. 3. In this experiment, we obtained image measurements at 3Hz and utilized COLMAP [21] for structure-from-motion. Cubic B-splines were adopted for the continuous-time state representation, with control node frequencies set to 5Hz for the pose spline and 0.2Hz for the IMU bias splines. To compare the effect of the measurement model, the anchor self-calibration was performed using model **A** and **B**, adjusting the cost function of (26) with each likelihood cost function.

Since the estimated results are expressed in a coordinate system defined by the COLMAP, we transformed them to the MOCAP coordinate system for accuracy evaluation by aligning the estimated state trajectory with the ground truth. The root mean squared errors (RMSE) of total anchor estimation results are presented in Table II. The orientation RMSE is computed by $(\frac{1}{N_a} \sum_{j=1}^{N_a} \|\angle(\mathbf{R}_j(\hat{\mathbf{R}}_j)^T)\|^2)^{\frac{1}{2}}$, where $\mathbf{R}_j$, $\hat{\mathbf{R}}_j$

denote the ground truth and estimate of the j-th anchor, and $\angle(\cdot)$ converts the rotation matrix to axis-angle representation.

In both environments, our measurement model **C** demonstrates the superior accuracy in position RMSE. However, we observed challenges in accurately estimating the anchor orientation solely based on the directional bias of anchors in UWB measurements. Nonetheless, this implies that even with errors in anchor's orientation, the accuracy of localization system for mobile platforms is not significantly compromised. In section V-C, we quantify the impact of these estimation errors on localization performance.

C. Filtering-based State Estimation

In Section V-A, we demonstrated that utilizing the asymmetric noise distribution effectively can capture error sources in UWB range measurements. This distribution can be integrated into a filtering-based state estimation method through the proposed iterative update algorithm. For measurement models using Gaussian noise, Huber norm-based update method can be employed to mitigate the effect of outliers [11]. We compared the estimation results of our method with standard extended Kalman filter (EKF) and Huber-norm based update method, as summarized in Table III. For the Huber norm-based update method, we modified the function $\psi(e)$ in (30) as

$$\psi(e) = \begin{cases} \frac{1}{\sigma^2}, & \text{for } |e| < \sigma, \\ \frac{1}{\sigma|e|}, & \text{otherwise.} \end{cases} \quad (37)$$

To ensure uniform calculation time suitable for real-time systems, we limited the maximum number of iterations to three, which proved adequate for convergence in our experiments. For the prediction step of the filter, we integrate IMU sensor readings based on [25].

We collected datasets comprising UWB and IMU measurements from the same experimental settings in Section V-
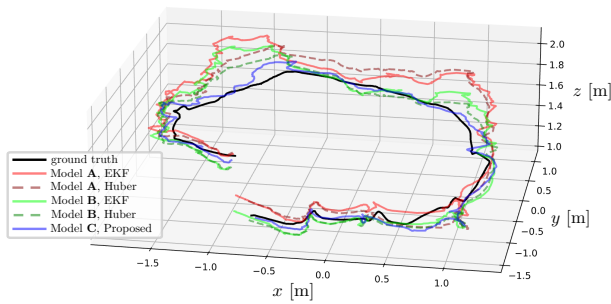
Fig. 6. The comparison of the estimated trajectories in Env. #2. For clarity, we visualize a portion of the trajectories.

TABLE III

COMPARISON OF POSITION RMSE FOR DIFFERENT MODELS AND UPDATE METHODS

Model	Method	Env. #1		Env. #2	
		ground truth	calibrated	ground truth	calibrated
A	EKF	17.5cm	16.9cm	22.2cm	19.9cm
A	Huber	15.4cm	15.7cm	20.9cm	18.5cm
B	EKF	13.7cm	14.2cm	17.3cm	17.3cm
B	Huber	12.1cm	12.4cm	15.0cm	15.3cm
C	Proposed	**9.7**cm	**10.7**cm	**13.1**cm	**13.6**cm

B. According to the update methods, we compared the estimation results with the ground truth. The comparison results are presented in Table III and visualized in Fig. 6.

Our proposed update method demonstrates superior performance, with a reduction in position RMSE ranging from 40% to 45% compared to the standard method. Additionally, we note that the RMSE of the state estimation results, obtained using the anchor setup estimated through anchor self-calibration in Section V-B, increases only by 4% to 10% compared to the results obtained using the actual setup.

VI. CONCLUSIONS

In this paper, we introduce a UWB-based localization system using a UWB range measurement model that accounts for antenna anisotropy and NLOS/multipath effects. We present a calibration method for our proposed model, demonstrating its efficacy in reducing measurement errors and capturing noise distribution. Furthermore, we validate its effectiveness on our proposed UWB-based localization system including continuous-time anchor self-calibration and filtering-based real-time state estimation.

As part of our future work, we intend to conduct a rigorous analysis of the proposed model alongside various models aimed at enhancing the accuracy of UWB measurements (e.g. [8]–[11]), focusing on both accuracy and computational efficiency metrics. In addition, we aim to expand our methodology beyond TWR-based UWB range measurements to encompass the time difference of arrival (TDOA) technique, exploring their potential benefits and applications.

REFERENCES

[1] J. Tiemann, F. Schweikowski, and C. Wietfeld, "Design of an uwb indoor-positioning system for uav navigation in gnss-denied environments," in *International Conference on Indoor Positioning and Ondoor Navigation*, 2015, pp. 1–7.

[2] T. H. Nguyen, T.-M. Nguyen, and L. Xie, "Tightly-coupled ultra-wideband-aided monocular visual slam with degenerate anchor configurations," *Autonomous Robots*, vol. 44, no. 8, pp. 1519–1534, 2020.

[3] Y. Cao and G. Beltrame, "Vir-slam: Visual, inertial, and ranging slam for single and multi-robot systems," *Autonomous Robots*, vol. 45, pp. 905–917, 2021.

[4] Y. Song, M. Guan, W. P. Tay, C. L. Law, and C. Wen, "Uwb/lidar fusion for cooperative range-only slam," in *International Conference on Robotics and Automation*, 2019, pp. 6568–6574.

[5] G. Wang and W. Kong, "Angle-dependent pulse distortion in uwb radiation and its impact on uwb impulse communications," *Electronics Letters*, vol. 41, no. 25, p. 1, 2005.

[6] R. Ye, S. Redfield, and H. Liu, "High-precision indoor uwb localization: Technical challenges and method," in *IEEE International Conference on Ultra-Wideband*, vol. 2, 2010, pp. 1–4.

[7] J. Tiemann, J. Pillmann, and C. Wietfeld, "Ultra-wideband antenna-induced error prediction using deep learning on channel response data," in *IEEE 85th Vehicular Technology Conference (VTC Spring)*, 2017, pp. 1–5.

[8] A. Ledergerber and R. D'Andrea, "Ultra-wideband range measurement model with gaussian processes," in *IEEE Conference on Control Technology and Applications*, 2017, pp. 1929–1934.

[9] A. Ledergerber and R. D'andrea, "Calibrating away inaccuracies in ultra wideband range measurements: A maximum likelihood approach," *IEEE Access*, vol. 6, pp. 78 719–78 730, 2018.

[10] W. Zhao, A. Goudar, J. Panerati, and A. P. Schoellig, "Learning-based bias correction for ultra-wideband localization of resource-constrained mobile robots," *arXiv preprint arXiv:2003.09371*, 2020.

[11] W. Zhao, J. Panerati, and A. P. Schoellig, "Learning-based bias correction for time difference of arrival ultra-wideband localization of resource-constrained mobile robots," *IEEE Robotics and Automation Letters*, vol. 6, no. 2, pp. 3639–3646, 2021.

[12] J. Khodjaev, Y. Park, and A. Saeed Malik, "Survey of nlos identification and error mitigation problems in uwb-based positioning algorithms for dense environments," *annals of telecommunications-annales des télécommunications*, vol. 65, pp. 301–311, 2010.

[13] V. Niculescu, D. Palossi, M. Magno, and L. Benini, "Energy-efficient, precise uwb-based 3-d localization of sensor nodes with a nano-uav," *IEEE Internet of Things Journal*, vol. 10, no. 7, pp. 5760–5777, 2022.

[14] M. Kok, J. D. Hol, and T. B. Schön, "Indoor positioning using ultrawideband and inertial measurements," *IEEE Transactions on Vehicular Technology*, vol. 64, no. 4, pp. 1293–1303, 2015.

[15] M. Ridolfi, A. Kaya, R. Berkvens, M. Weyn, W. Joseph, and E. D. Poorter, "Self-calibration and collaborative localization for uwb positioning systems: A survey and future research directions," *ACM Computing Surveys*, vol. 54, no. 4, pp. 1–27, 2021.

[16] C. Hu, P. Huang, and W. Wang, "Tightly coupled visual-inertial-uwb indoor localization system with multiple position-unknown anchors," *IEEE Robotics and Automation Letters*, 2024.

[17] P. Lutz, M. J. Schuster, and F. Steidle, "Visual-inertial slam aided estimation of anchor poses and sensor error model parameters of uwb radio modules," in *19th International Conference on Advanced Robotics*, 2019, pp. 739–746.

[18] C. An, X. Chen, I. H. Sloan, and R. S. Womersley, "Regularized least squares approximations on the sphere using spherical designs," *SIAM Journal on Numerical Analysis*, vol. 50, no. 3, pp. 1513–1534, 2012.

[19] G. Cioffi, T. Cieslewski, and D. Scaramuzza, "Continuous-time vs. discrete-time vision-based slam: A comparative study," *IEEE Robotics and Automation Letters*, vol. 7, no. 2, pp. 2399–2406, 2022.

[20] S. Lovegrove, A. Patron-Perez, and G. Sibley, "Spline fusion: A continuous-time representation for visual-inertial fusion with application to rolling shutter cameras," in *British Machine Vision Conference*, 2013.

[21] J. L. Schonberger and J.-M. Frahm, "Structure-from-motion revisited," in *Proceedings of the IEEE Conference on Computer Vision and Pattern Recognition*, 2016, pp. 4104–4113.

[22] B. Kovačević, Ž. urović, and S. Glavaški, "On robust kalman filtering," *International Journal of Control*, vol. 56, no. 3, pp. 547–562, 1992.

[23] D. J. MacKay, *Information theory, inference and learning algorithms*. Cambridge university press, 2003.

[24] S. Agarwal *et al.*, "Ceres Solver." [Online]. Available: https://ceres-solver.org

[25] J. Sola, "Quaternion kinematics for the error-state kalman filter," *arXiv preprint arXiv:1711.02508*, 2017.